Chinese Chemical Letters 37 (2026) 111883

Contents lists available at ScienceDirect

Chinese Chemical Letters

journal homepage: www.elsevier.com/locate/cclet

In situ growth of redox-active covalent organic frameworks on aminated MXene for functional separator coatings in lithium-sulfur batteries

Kehan Tang[1], Peiwen Xu[1], Xinyuan Wu, Youlong Zhu*

Key Laboratory for Polymeric Composite and Functional Materials of Ministry of Education, IGCME, School of Chemistry, Sun Yat-sen University, Guangzhou 510006, China

ARTICLE INFO

Article history:
Received 25 July 2025
Revised 16 September 2025
Accepted 23 September 2025
Available online 23 September 2025

Keywords:
Covalent organic frameworks
Functional coating
Separator
Lithium-sulfur batteries
Hybrid materials
MXene

ABSTRACT

Lithium-sulfur (Li-S) batteries are considered as one of the most promising next-generation energy storage systems owing to their high theoretical capacity and energy density. However, conventional polyolefin-based separators suffer from randomly distributed pores with broad size distributions, which are ineffective in suppressing the polysulfide shuttle effect. Moreover, they lack functional groups for catalyzing polysulfides conversion and promoting uniform lithium-ion deposition. Herein, we synthesized a hybrid material (denoted as DAAQ-TFP/MXene) *via in situ* growth of redox-active covalent organic frameworks (DAAQ-TFP) on amine-functionalized MXene nanosheets. The resulting DAAQ-TFP/MXene hybrid features a porous architecture and dual binding/catalytic sites, enabling efficient polysulfides adsorption and catalytic conversion, enhanced lithium-ion transport, and uniform lithium deposition. Consequently, the DAAQ-TFP/MXene-coated PP separator exhibits a high lithium-ion transference number (0.53). The Li||Li symmetric cell incorporating this separator operates stably for 3800 h at 5 mA/cm^2 and 1 mAh/cm^2. Furthermore, Li-S full cells using DAAQ-TFP/MXene@PP separator delivers a high specific capacity (1224 mAh/g at 0.1 C), excellent rate performance (631 mAh/g at 5 C), and long-term cycling stability (71.3 % capacity retention after 300 cycles at 1 C). This study provides a promising strategy for designing MXene-COF hybrid materials as functional coatings to improve the performance of Li-S batteries.

© 2026 Published by Elsevier B.V. on behalf of Chinese Chemical Society and Institute of Materia Medica, Chinese Academy of Medical Sciences.

As one of the most promising next-generation high-energy-density battery technologies, lithium-sulfur (Li-S) batteries possess high theoretical capacity (1675 mAh/g) and energy density (2600 Wh/kg) as well as abundant natural sulfur element [1–5]. However, several critical challenges hinder their practical application, particularly in terms of capacity retention and cycle life. These issues include the notorious lithium polysulfides (LiPSs) shuttle effect, the inherently low electrical conductivity of sulfur, and sluggish redox kinetics of sulfur species [6,7]. On the cathode side, the complicated multiphase reactions and high energy barrier associated with the liquid-solid phase conversion significantly slow down the sulfur redox kinetics [8–10]. Meanwhile, the current commercial polyolefin separators with random and broad pore size distributions are unable to suppress the shuttle effect of soluble LiPSs during the charge-discharge process [11–14], resulting in rapid capacity decay of the battery. On the anode side, lithium metal is prone to dendritic growth caused by uneven lithium deposition, which can lead to internal short circuits and, in severe cases, combustion or explosion [1,15]. To address these issues, considerable efforts have been devoted to modify the commercial polyolefin separators to improve their electrochemical performance and suppress the shuttle effect.

Introducing functional coatings on the cathode-facing side of the separator in Li-S batteries has emerged as an effective strategy to suppress the shuttle effect of LiPSs [16–20]. Conductive carbon-based materials, such as carbon nanotubes, graphene, and porous carbon aerogels, have been widely explored owing to their high conductivity and large specific surface area [21,22]. However, they generally exhibit limited catalytic activity toward sulfur redox reactions because of limited functional moieties, which hampers their ability to accelerate the sulfur oxidation–reduction kinetics [23]. Transition metal-based compounds with inherent electrocatalytic activity have been incorporated into the functional coatings [24,25], including transition metal oxides (TMOs) [26,27], transition metal phosphides (TMPs) [28], transition metal nitrides (TMNs) [29], transition metal carbides (TMCs) [30–32], transition

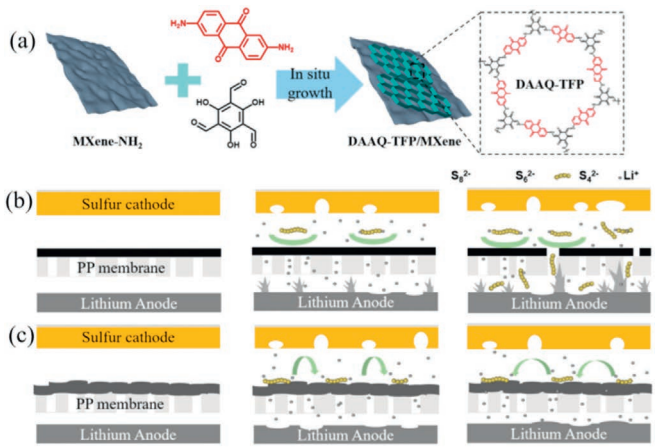
* Corresponding author.
E-mail address: zhuyl9@mail.sysu.edu.cn (Y. Zhu).
[1] These authors contributed equally to this work.

https://doi.org/10.1016/j.cclet.2025.111883
1001-8417/© 2026 Published by Elsevier B.V. on behalf of Chinese Chemical Society and Institute of Materia Medica, Chinese Academy of Medical Sciences.

metal sulfides (TMSs) [33,34], transition metal compounds-based hybrids [35–37], metal-organic frameworks (MOFs) [38–40], and single atom catalysts [41–43]. These catalysts were typically combined with high specific surface area materials to provide abundant active sites for anchoring and catalyzing the conversion of LiPSs, thereby accelerating the kinetics of sulfur redox process [44,45]. However, due to the lack of lithiophilic sites, many of these materials struggle to facilitate uniform lithium ion transport, which is crucial for suppressing lithium dendrite growth [46]. Covalent organic framework (COFs), composed of lightweight elements and featuring tunable structures, high specific surface area, and excellent chemical/thermo stability [47,48]. Their unique pore structure and multiple functional groups allow for the electrostatic adsorption or repulsion of polysulfides, effectively mitigating the shuttle effect [49–55]. Furthermore, COF-based functional coatings can serve as lithium-ion transport channels enriched with lithiophilic groups, enabling more uniform ion distribution [56–60]. Nevertheless, the inherent poor conductivity of COFs limits their utilization efficiency for active polysulfides [61]. Therefore, the development of multifunctional COF-based composite coatings that combine good electrical conductivity, high catalytic activity, large surface area, and abundant lithiophilic sites is key to achieving high specific capacity, enhanced safety, and long cycle life in advanced Li-S batteries.

Herein, we report the synthesis of a COF/MXene hybrid material (denoted as DAAQ-TFP/MXene), constructed by *in situ* growth of an anthraquinone-based COF (DAAQ-TFP) on amine-modified transition metal carbides (MXene). This hybrid was subsequently employed as a functional coating to decorate commercial polypropylene (PP) separators, yielding DAAQ-TFP/MXene@PP, which was then applied in Li-S batteries. In this functional separator, the active metal sites of MXene and the redox-active anthraquinone units in DAAQ-TFP serve as dual anchors, synergistically catalyzing the redox conversion of LiPSs. The covalent linkage between MXene and the DAAQ-TFP enhances the conductivity of the hybrid material. Meanwhile, the microporous structure of DAAQ-TFP promotes effective physical adsorption of LiPSs, thereby mitigating the shuttle effect and enabling synergistic adsorption-catalysis performance. Additionally, the ordered pore channels and abundant lithiophilic sites in the DAAQ-TFP COF, such as carbonyl groups, β-ketoamine linkages, and anthraquinone moieties, can facilitate uniform and efficient lithium-ion transport. As a result, Li-S batteries assembled with DAAQ-TFP/MXene@PP separators exhibited a high specific capacity of 1224 mAh/g at 0.1 C, excellent rate performance (631 mAh/g at 5 C), and outstanding long-term cycling stability. Moreover, Li/Li symmetric cells using the same modified separator demonstrated stable cycling for over 3800 h at a current density of 5 mA/cm^2 and an areal capacity of 1 mAh/cm^2. This study offers a new approach for developing functional separator coatings toward high-performance Li-S batteries.

DAAQ-TFP/MXene was synthesized *via* an *in situ* growth strategy, as illustrated in Scheme 1. First, amine-modified MXene nanosheets (MXene-NH_2) were prepared by reacting diazonium salt with MXene. Subsequently, a Schiff-base reaction between triformylphloroglucinol (TFP) and 2,6-diaminoanthraquinone (DAAQ) in the presence of MXene-NH_2 led to the *in situ* growth of the anthraquinone-based COF (DAAQ-TFP) on the MXene-NH_2 surface. Prior to the reaction, MXene-NH_2 exhibited a typical two-dimensional sheet-like morphology with a smooth and flat surface (Fig. 1a). After polymerization, SEM images revealed the presence of distinct COF nanoparticles uniformly distributed on the surface of MXene nanosheets (Figs. 1b and c). The chemical and crystalline structures of the resulting DAAQ-TFP/MXene hybrid were further characterized by Fourier transform infrared spectroscopy (FT-IR) and powder X-ray diffraction (PXRD). As shown in Fig. 1d, the FT-IR of DAAQ monomer displays N–H stretching vibration



Scheme 1. (a) Schematic illustration of the *in situ* growth of DAAQ-TFP on MXene-NH_2 to prepare DAAQ-TFP/MXene hybrid. Comparison of the polysulfide shuttle effect and lithium-ion transport during the discharge/charge process in Li-S batteries using separators with (b) non-catalytic functional coatings and (c) the DAAQ-TFP/MXene hybrid materials.

peaks at 3332 and 3421 cm^{-1}. After the polymerization, the intensity of N–H peaks significantly decreased, and a characteristic C–N stretching peak appeared at 1255 cm^{-1}, corresponding to the formation of β-ketoamine linkages from the condensation reaction between aldehyde and amine groups followed by the tautomerization. These changes confirm the successful polymerization between TFP and DAAQ. Additionally, PXRD analysis confirmed that the crystalline structure of the DAAQ-TFP COF was preserved in the DAAQ-TFP/MXene hybrid, the diffraction peaks are consistent with the literature reported (Fig. S1 in Supporting information) [62]. These results collectively demonstrate the successful *in situ* growth of DAAQ-TFP on MXene-NH_2. Nitrogen adsorption–desorption measurements (Fig. 1e) was carried out to study their porosities, both materials exhibited typical combination of type I and type IV isotherms. The BET surface area of DAAQ-TFP/MXene is calculated to be 761.4 m^2/g, which is lower than that of pristine DAAQ-TFP (1154.3 m^2/g) due to the incorporation of nearly non-porous MXene-NH_2. Non local density functional theory (NLDFT) pore size analysis indicated that both materials possess similar hierarchical porosity, with dominant pore sizes centered at approximately 1.9 and 4.8 nm (Fig. 1f). This combination of micropores and mesopores is beneficial for PSs adsorption, suppression of the shuttle effect, and improved ion transport.

The DAAQ-TFP/MXene hybrid, DAAQ-TFP, and MXene materials were individually mixed with carbon black and binder in *N*-methyl-2-pyrrolidone (NMP). After thorough grinding, the resulting slurries were uniformly coated onto PP membranes *via* a simple blade-coating process to prepare functional separators, denoted as DAAQ-TFP/MXene@PP, DAAQ-TFP@PP, and MXene@PP, respectively. A digital photograph of the DAAQ-TFP/MXene@PP separator was presented in Fig. 2a. The thickness of the DAAQ-TFP/MXene in the composite separator is about 3 µm (Fig. 2b). SEM images revealed that the top surface of DAAQ-TFP/MXene@PP exhibited a dense and continuous layer formed by DAAQ-TFP/MXene (Fig. 2c), while the uncoated bottom side maintained the original porous morphology of the pristine PP membrane (Fig. 2d). The electrolyte affinity of the modified and unmodified separators was evaluated *via* optical contact angle measurements. Benefiting from the abundant polar functional groups in the DAAQ-TFP and the metal sites introduced by the MXene nanosheets, the DAAQ-TFP/MXene@PP separator demonstrated excellent wettability with the Li-S electrolyte. As shown in Fig. 2e, the contact angle of DAAQ-TFP/MXene@PP was only 13°, significantly lower than that of the pristine PP membrane

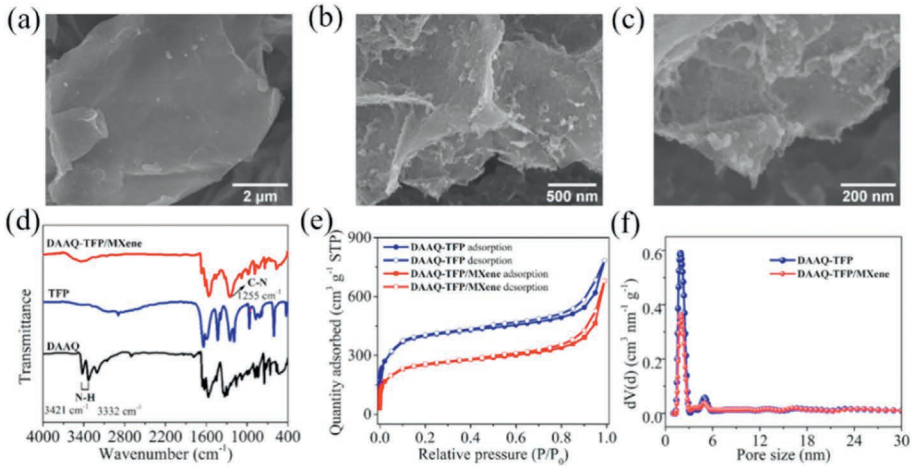


Fig. 1. (a) SEM image of MXene. (b, c) The SEM images of DAAQ-TFP/MXene at different magnifications. (d) FT-IR spectra of DAAQ-TFP/MXene, TFP, and DAAQ. (e) N_2 adsorption-desorption isotherms of DAAQ-TFP and DAAQ-TFP/MXene measured at 77 K. (f) Pore size distribution curves of DAAQ-TFP and DAAQ-TFP/MXene.

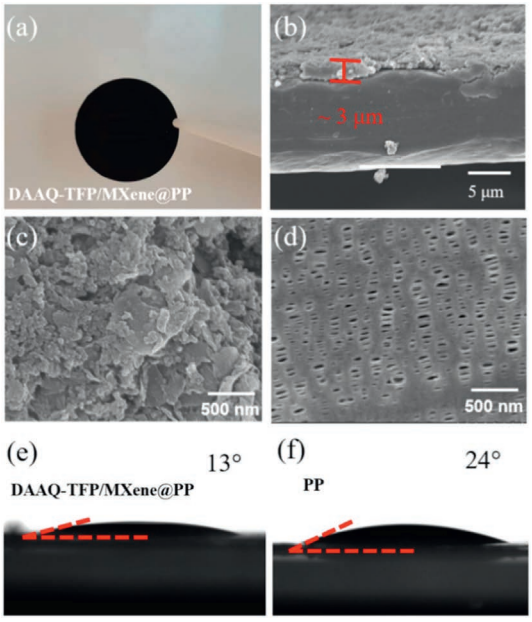


Fig. 2. (a) Digital photograph and (b) cross-sectional SEM image of the DAAQ-TFP/MXene@PP separator. (c) Top-view and (d) bottom-view SEM images of the DAAQ-TFP/MXene@PP separator. Contact angle measurement of (e) the DAAQ-TFP/MXene@PP and (f) pristine PP separator.

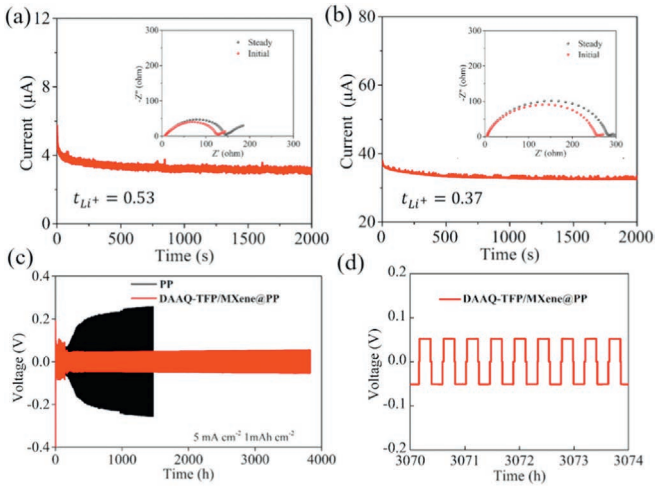


Fig. 3. Chronoamperometry profiles of Li/Li symmetric cells using (a) DAAQ-TFP/MXene@PP and (b) pristine PP separators under a polarization voltage of 10 mV (insets: corresponding impedance spectra before and after polarization). (c) Voltage-time profile of Li/Li symmetric cells with DAAQ-TFP/MXene@PP and pristine PP separators at a current density of 5 mA/cm^2 and an areal capacity of 1 mAh/cm^2. (d) Enlarged voltage-time profile of Li/Li symmetric cell with DAAQ-TFP/MXene@PP separator during the cycling interval from 3070 h to 3074 h.

(24°, Fig. 2f). Enhanced electrolyte affinity is critical for lowering internal resistance and promoting efficient ion transport within the battery.

The lithium-ion transference number (t_{Li^+}) is a critical parameter for evaluating the lithium-ion transport efficiency of modified separators. Li/Li symmetric cells were assembled using both DAAQ-TFP/MXene@PP and pristine PP membranes. The t_{Li^+} value of the DAAQ-TFP/MXene@PP separator was determined to be 0.53, which is significantly higher than that of the unmodified PP membrane with only 0.37 (Figs. 3a and b). This enhancement can be attributed to the high porosity of DAAQ-TFP/MXene hybrid and the presence of abundant lithium-affinitive functional groups in DAAQ-TFP, which collectively provide rapid ion-conduction pathways and improve lithium-ion transport efficiency. Furthermore, constant current charge-discharge experiments were conducted on Li/Li symmetric cells assembled with DAAQ-TFP/MXene@PP and PP membrane under a current density of 5 mA/cm^2 and an areal capacity of 1 mAh/cm^2 to investigate the stability of lithium metal deposition/stripping. The Li/Li symmetric cells based on DAAQ-TFP/MXene@PP exhibited stable lithium deposition/stripping behavior and lower overpotential, achieving continuous cycling for 3800 h under these conditions (Figs. 3c and d). In contrast, cells based on the pristine PP membrane displayed a much higher overpotential and a significantly shorter cycling lifespan, underscoring the superior lithium-ion transport capability of the functionalized separator.

To demonstrate the superior electrochemical performance of DAAQ-TFP/MXene@PP separator in Li-S batteries, a series of Li-S cells were assembled using DAAQ-TFP/MXene@PP, DAAQ-TFP@PP, MXene@PP, and pristine PP membranes, with the modified coatings facing the sulfur cathode. Cyclic voltammetry (CV) curves were tested at a scan rate of 0.1 mV/s within the voltage range of 1.7–2.8 V (Fig. 4a). Among the four configurations, the Li-S battery employing the DAAQ-TFP/MXene@PP separator exhibited the highest peak currents, along with a noticeable positive shift in the reduction peak and a negative shift in the oxidation peak. The

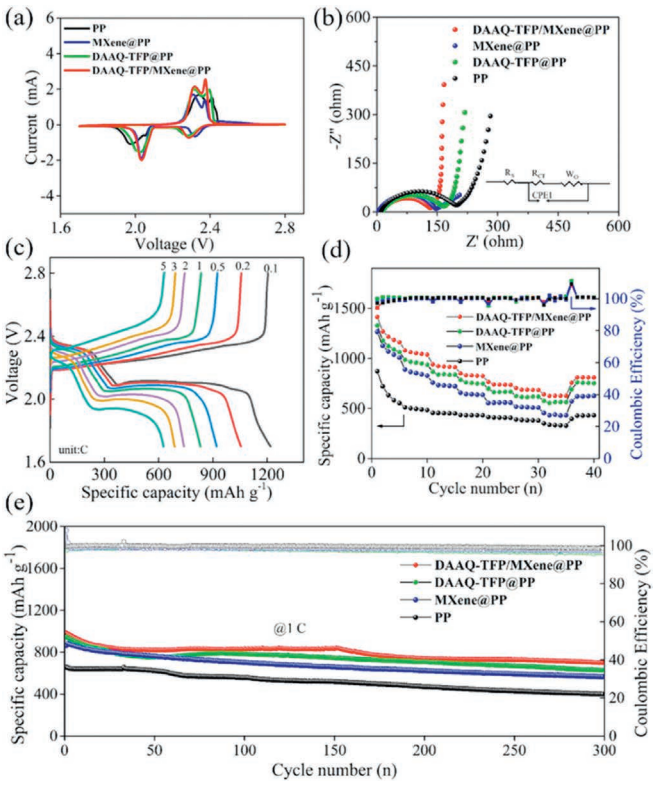


Fig. 4. (a) Cyclic voltammetry curves and (b) Nyquist plots of the Li-S batteries using DAAQ-TFP/MXene@PP, DAAQ-TFP@PP, MXene@PP, and pristine PP separators. (c) Galvanostatic charge-discharge profiles of Li-S batteries with DAAQ-TFP/MXene@PP separator at various current densities. (d) Rate performance and (e) cycling performance at 1 C of Li-S batteries using DAAQ-TFP/MXene@PP, DAAQ-TFP@PP, MXene@PP, and pristine PP separators.

CV curves of symmetric cells using DAAQ-TFP/MXene@PP separator exhibited the largest redox peak current and smallest polarization voltage among Li-S symmetric cells with DAAQ-TFP@PP or pristine PP separators (Fig. S3 in Supporting information). Furthermore, Tafel analysis was performed to evaluate their catalytic behavior. The exchange current density (I_o) derived from the Tafel plot fitting revealed that the Li-S battery with the DAAQ-TFP/MXene@PP separator achieved the highest I_o value of 0.381 mA/cm^2, surpassing those of the DAAQ-TFP@PP-based (0.371 mA/cm^2) and pristine PP-based (0.311 mA/cm^2) Li-S battery at a scan rate 50 mV/s (Fig. S4 in Supporting information). These results indicate accelerated redox kinetics, reduced polarization, and enhanced catalytic activity toward polysulfide conversion. Furthermore, electrochemical impedance spectroscopy (EIS) was performed at the open-circuit voltage, and the equivalent circuit diagram was also provided to evaluate charge transfer resistance (Fig. 4b). The corresponding fitted impedance parameters are summarized in Table S1 (Supporting information). The Nyquist plots consist of the electrolyte/electrode interface resistance (R_S), charge transfer resistance (R_{CT}), and Warburg impedance (W_O) [63,64]. All Li-S batteries with different separators exhibited small R_S values, indicating their good electrolyte/electrode compatibility. Compared to the pristine PP separator, all modified separators showed reduced R_{CT} values. Notably, the DAAQ-TFP/MXene@PP-based cell displayed the lowest R_{CT}, underscoring the synergistic effect of DAAQ-TFP and MXene in promoting efficient charge transfer and ion diffusion across the separator, which also suppressing the PSs shuttling.

The rate performance of Li-S batteries assembled with DAAQ-TFP/MXene@PP, DAAQ-TFP@PP, MXene@PP, and pristine PP separators was evaluated at under various current densities. All batteries exhibited typical charge/discharge profiles with one charging plateau and two distinct discharge plateaus, corresponding to the stepwise oxidation of Li_2S_2/Li_2S to S_8 and the stepwise reduction of S_8 to Li_2S_2/Li_2S (Fig. 4c and Fig. S5 in Supporting information). At 0.2 C, the charge/discharge profiles (Fig. S6 in Supporting information) reveal that the DAAQ-TFP/MXene@PP-based cell exhibited and a lower polarization voltage (254.7 mV) compared to the cells with DAAQ-TFP@PP (258.6 mV), MXene@PP (261.9 mV), or PP (268.7 mV) separators, indicating the fast reaction kinetics of DAAQ-TFP/MXene@PP-based Li-S battery. Additionally, DAAQ-TFP/MXene@PP-based cell exhibited a longer discharge plateau compared to cells with other separator, the discharge curves can be divided into high discharge plateaus (Q_H) and low discharge plateaus (Q_L), which are corresponding to the conversions of S_8 to long-chain LiPSs and LiPSs to Li_2S_2/Li_2S, respectively [65]. The DAAQ-TFP/MXene@PP-based cell delivers a markedly higher Q_H capacity than the other separator-based batteries (Fig. S7 in Supporting information), suggesting an accelerated transformation of S_8 to PSs. Since S_8 is often encapsulated by Li_2S_2/Li_2S during discharge-limiting sulfur utilization-the high Q_H capacity further confirms that Li_2S_2 is efficiently converted back to S_8, catalyzed by the DAAQ-TFP/MXene@PP layer. Among the four Li-S batteries, the DAAQ-TFP/MXene@PP-based Li-S battery consistently achieves the highest specific capacities across all tested current rates, demonstrating its superior rate performance (Fig. 4d). Specifically, the DAAQ-TFP/MXene@PP-based Li-S battery achieved reversible capacities of 1224, 1058, 925, 834, 744, 691 and 631 mAh/g at 0.1, 0.2, 0.5, 1, 2, 3, and 5 C, respectively. When the current was restored to 1 C, the capacity recovered to 819 mAh/g, indicating excellent structure stability and rate reversibility. To further evaluate the long-term cycling performance, Li-S batteries with the four different separators were tested at 1 C for 300 cycles (Fig. 4e). The Li-S battery employing the DAAQ-TFP/MXene@PP separator delivered an initial discharge capacity of 985 mAh/g and the capacity retention rate was 71.3 % after 300 cycles, with an average capacity decay rate of only 0.096 % per cycle. In contrast, the Li-S battery assembled with pristine PP membrane exhibited a lower initial discharge specific capacity of 768.3 mAh/g and a capacity retention rate of only 63.2 % after 300 cycles, corresponding to a higher average decay rate of 0.12 % per cycle. These results confirm that the DAAQ-TFP/MXene@PP separator imparts excellent rate performance and cycling stability to Li-S batteries. This can be attributed to its synergistic adsorption-catalysis properties, stemming from the combination of a porous COF and dual catalytic sites. Additionally, the mesoporous structure and interconnected channels formed by stacked nanosheets of MXene facilitate rapid lithium-ion diffusion, further enhancing electrochemical performance.

To further validate the adsorption-catalysis performance and highlight the advantages of the DAAQ-TFP/MXene hybrid material, LiPSs adsorption experiments (Li_2S_6 was used as model PSs) were conducted to compare the adsorption kinetics of different samples. Specifically, 10 mg of each sample was added to 3 mL of 5 mmol/L Li_2S_6 solution and allowed to stand for 24 h (Figs. S8a-d in Supporting information). Upon addition of MXene or DAAQ-TFP, the solution color changed from the original yellow-brown to a darker brown, indicating partial Li_2S_6 adsorption. Notably, the solution containing the DAAQ-TFP/MXene hybrid underwent significant decolorization, suggesting its superior adsorption capability. Subsequently, the supernatants were analyzed using UV–visible spectroscopy (Fig. S8e in Supporting information). Compared to the characteristic Li_2S_6 absorbance peak at ~412 nm observed in the blank solution, all samples showed reduced peak intensities, with varying degrees of attenuation. The DAAQ-TFP sample exhibited a notably lower absorbance than MXene, attributable to its high porosity and strong interactions between anthraquinone moieties and Li_2S_6. Remarkably, the Li_2S_6 solution treated with the DAAQ-

TFP/MXene hybrid showed an almost complete disappearance of the absorption peak, underscoring the synergistic effect of dual catalytic sites and the porous structure in enhancing adsorption-catalysis performance.

In summary, a redox-active covalent organic framework/MXene hybrid (DAAQ-TFP/MXene) was successfully synthesized *via* an *in situ* growth strategy. The resulting DAAQ-TFP/MXene was subsequently coated onto a commercial PP membrane to fabricate a functional separator, denoted as DAAQ-TFP/MXene@PP. The porous structure of DAAQ-TFP enables effective adsorption of LiPSs, while the metal-active sites of MXene and the anthraquinone moieties within DAAQ-TFP synergistically catalyze LiPSs conversion, thereby enhancing sulfur redox kinetics. In addition, the abundant polar functional groups in DAAQ-TFP, along with the pore channels formed by the stacking of MXene nanosheets, facilitate efficient lithium-ion transport. As a result, the DAAQ-TFP/MXene@PP modified separator can simultaneously suppress shuttle effects of LiPSs and promote uniform lithium deposition and stripping. Li||Li symmetric cells assembled with this modified separator can stably cycle for 3800 h under conditions of 5 mA/cm^2 and 1 mAh/cm^2. Moreover, Li-S full batteries employing DAAQ-TFP/MXene@PP separator demonstrate a high specific capacity of 1224 mAh/g at 0.1 C, excellent rate capability (631 mAh/g at 5 C), and outstanding cycling performance with a capacity retention of 71.3 % after 300 cycles at 1 C. This work presents a facile and effective strategy for constructing COF/MXene hybrids as functional separator coatings, offering a promising route toward high-performance Li-S batteries.

Declaration of competing interest

The authors declare that they have no known competing financial interests or personal relationships that could have appeared to influence the work reported in this paper.

CRediT authorship contribution statement

Kehan Tang: Writing – original draft, Methodology, Investigation, Formal analysis, Data curation. **Peiwen Xu:** Methodology, Investigation, Formal analysis, Data curation. **Xinyuan Wu:** Formal analysis, Data curation. **Youlong Zhu:** Writing – review & editing, Investigation, Funding acquisition, Conceptualization.

Acknowledgments

This work is financial supported by the projects of National Natural Science Foundation of China (No. 52103328), Guangzhou Science and Technology Programme (No. 2024A04J9960), and Guangdong Basic Research Center of Excellence for Functional Molecular Engineering.

Supplementary materials

Supplementary material associated with this article can be found, in the online version, at doi:10.1016/j.cclet.2025.111883.

References

[1] Q. Cheng, Z.X. Chen, X.Y. Li, et al., Adv. Energy Mater. 13 (2023) 2301770.
[2] Y. Mo, L. Liao, D. Li, et al., Chin. Chem. Lett. 34 (2023) 107130.
[3] H. Pan, Z. Cheng, Z. Zhou, et al., Nano-Micro Lett. 15 (2023) 165.
[4] Y. Fei, G. Li, Adv. Funct. Mater. 34 (2024) 2312550.
[5] S.C. Kim, X. Gao, S.L. Liao, et al., Nat. Commun. 15 (2024) 1268.
[6] X.Y. Li, S. Feng, M. Zhao, et al., Angew. Chem. Int. Ed. 134 (2022) e202114671.
[7] J. Li, L. Gao, F. Pan, et al., Nano-Micro Lett. 16 (2024) 12.
[8] R. Liu, Z. Wei, L. Peng, et al., Nature 626 (2024) 98–104.
[9] Z. Wang, Y. Li, H. Ji, et al., Adv. Mater. 34 (2022) 2203699.
[10] W. Yao, K. Liao, T. Lai, H. Sul, A. Manthiram, Chem. Rev. 124 (2024) 4935–5118.
[11] L. Wang, W. Hua, X. Wan, et al., Adv. Mater. 34 (2022) 2110279.
[12] L. Wang, Z. Hu, X. Wan, et al., Adv. Energy Mater. 12 (2022) 2200340.
[13] X. Gao, Z. Yu, J. Wang, et al., Proc. Natl. Acad. Sci. U. S. A. 120 (2023) e2301260120.
[14] T. Wang, J. He, Z. Zhu, et al., Adv. Mater. 35 (2023) 2303520.
[15] R. Gao, M. Zhang, Z. Han, et al., Adv. Mater. 36 (2024) 2303610.
[16] Z. Zhao, Y. Pan, H. Chen, et al., Adv. Funct. Mater. 34 (2024) 2402182.
[17] W. Jin, Y. Guo, T. Gan, et al., Angew. Chem. Int. Ed. 64 (2025) e202420544.
[18] Y. Wang, X. Yang, P. Li, et al., Macromol. Rapid Commun. 44 (2023) 2200760.
[19] M.K. Aslam, S. Jamil, S. Hussain, M. Xu, Energy Environ. Mater. 6 (2023) e12420.
[20] A. Kim, S.H. Oh, A. Adhikari, et al., J. Mater. Chem. A 11 (2023) 7833–7866.
[21] J. Huang, K. Leng, Z. Cen, et al., Sci. China Mater. 66 (2023) 1747–1756.
[22] T. Wang, K. Kretschmer, S. Choi, et al., Small Methods 1 (2017) 1700089.
[23] J. Qin, R. Wang, P. Xiao, D. Wang, Adv. Energy Mater. 13 (2023) 2300611.
[24] Q. Liang, S. Wang, Y. Yao, P. Dong, H. Song, Adv. Funct. Mater. 33 (2023) 2300825.
[25] C. Shi, J. Huang, Y. Tang, et al., Carbon. 202 (2023) 59–65.
[26] X. Liang, C.Y. Kwok, F. Lodi-Marzano, et al., Adv. Energy Mater. 6 (2016) 1501636.
[27] Z. Ma, Z. Qi, G. Song, et al., Adv. Funct. Mater. 34 (2024) 2403101.
[28] S. Huang, E. Huixiang, Y. Yang, et al., J. Mater. Chem. A 9 (2021) 7458–7480.
[29] S. Gu, H. Jiang, X. Li, et al., Energy Storage Mater. 53 (2022) 32–41.
[30] J.L. Cheong, C. Hu, W. Liu, et al., Nano Energy 102 (2022) 107659.
[31] M. Zhao, P. Tan, D. Cai, et al., Adv. Funct. Mater. 33 (2023) 2211505.
[32] Z.U. Rehman, K. Khan, S. Yao, et al., Mater. Today Chem. 40 (2024) 102200.
[33] B. Yan, X. Li, W. Xiao, et al., J. Mater. Chem. A 8 (2020) 17848–17882.
[34] S. Tian, G. Liu, S. Xu, et al., Adv. Funct. Mater. 34 (2024) 2309437.
[35] R. Wang, C. Ma, C. Li, et al., J. Energy Storage 109 (2025) 115168.
[36] Y. Chen, C. Ma, Z. Li, et al., Electrochim. Acta 517 (2025) 145762.
[37] D. Li, H. Sun, C. Ma, et al., J. Energy Storage 113 (2025) 115698.
[38] F. Qi, Z. Sun, X. Fan, et al., Adv. Energy Mater. 11 (2021) 2100387.
[39] R. Razaq, M.M.U. Din, D.R. Småbråten, et al., Adv. Energy Mater. 14 (2024) 2302897.
[40] P. Feng, W. Hou, Z. Bai, et al., Chin. Chem. Lett. 34 (2023) 107427.
[41] X. Zhang, T. Yang, Y. Zhang, et al., Adv. Mater. 35 (2023) 2208470.
[42] C. Zhou, M. Li, N. Hu, et al., Adv. Funct. Mater. 32 (2022) 2204635.
[43] Y. Miao, Y. Zheng, F. Tao, et al., Chin. Chem. Lett. 34 (2023) 107121.
[44] J. Wu, T. Ye, Y. Wang, et al., ACS Nano 16 (2022) 15734–15759.
[45] B. Liu, H. Gu, J.F. Torres, Z. Yin, A. Tricoli, Energy Environ. Sci. 17 (2024) 1073–1082.
[46] W. Yao, J. Xu, L. Ma, et al., Adv. Mater. 35 (2023) 2212116.
[47] S. Haldar, A. Schneemann, S. Kaskel, J. Am. Chem. Soc. 145 (2023) 13494–13513.
[48] Y.L. Zhu, Q.S. Bai, S. Ouyang, Y.H. Jin, W. Zhang, ChemSusChem 17 (2024) e202301118.
[49] Q. An, L. Wang, G. Zhao, et al., Adv. Mater. 36 (2024) 2305818.
[50] P. Li, H. Lv, Z. Li, et al., Adv. Mater. 33 (2021) 2007803.
[51] Z. Cheng, H. Pan, H. Zhong, et al., Adv. Funct. Mater. 28 (2018) 1707597.
[52] D. Luo, M. Li, Q. Ma, et al., Chem. Soc. Rev. 51 (2022) 2917–2938.
[53] X. Kang, T. He, R. Zou, et al., Small 20 (2024) 2306503.
[54] X. Liu, X.R. Sun, R. Yan, et al., Adv. Funct. Mater. 35 (2025) 2505986.
[55] X. Chen, H. Jiang, J.H. Liu, et al., Adv. Funct. Mater. 35 (2025) 2421697.
[56] X. Wu, S. Zhang, X. Xu, et al., Angew. Chem. Int. Ed. 63 (2024) e202319355.
[57] J. Xu, S. An, X. Song, et al., Adv. Mater. 33 (2021) 2105178.
[58] G. Yu, Y. Cui, S. Lin, et al., Adv. Funct. Mater. 34 (2024) 2314935.
[59] J. Duan, K. Wang, L. Teng, et al., ACS Nano 18 (2024) 29189–29202.
[60] S. Gullace, M. Abruzzese, L. Cusin, et al., J. Mater. Chem. A 12 (2024) 25359–25370.
[61] B. Hu, J. Xu, Z. Fan, et al., Adv. Energy Mater. 13 (2023) 2203540.
[62] C.R. DeBlase, K.E. Silberstein, T.T. Truong, H.D. Abruna, W.R. Dichtel, J. Am. Chem. Soc. 135 (2013) 16821–16824.
[63] C. Zhang, C. Ma, W. Zhang, et al., Chem. Eng. J. 481 (2024) 148374.
[64] S. Yao, H. Liu, C. Zhang, et al., J. Energy Storage 78 (2024) 110087.
[65] Y. Song, Y. Sun, L. Chen, et al., Adv. Funct. Mater. 34 (2024) 2409748.